Amino acid-appended pyromellitic diimide liquid materials, their photoluminescence, and thermal response turning photoluminescence off

Takumi Omura,[a][b] Shogo Morisako,[a] Kyosuke Isoda*[a]

[a] Organic Materials Chemistry Group, Sagami Chemical Research Institute, 2743-1 Hayakawa, Ayase, Kanagawa 252-1193, Japan

E-mail: k-isoda@sagami.or.jp

[b] Division of Molecular Sciences, Graduate School of Science, Kitasato University, 1-15-1 Kitasato Minami-ku, Sagamihara, Kanagawa, 252-0373, Japan

S0. Author Contributions

Takumi Omura: Experiments. **Shogo Morisako**: Single crystal X- ray Analysis and DFT calculations. **Kyosuke Isoda**: Writing - original draft, Supervision, Project administration, Funding acquisition.

S1. Experimental Procedures

General remarks

The ^{1}H and ^{13}C NMR spectra were recorded on a Bruker Ascend^{TM} Avance III HD 400MHz or UltraShield Plus 400 MHz NMR spectrometers (^{1}H: 400 MHz, ^{13}C: 101 MHz). All the spectroscopic measurements were carried out at room temperature. The chemical shifts of the ^{1}H and ^{13}C NMR signals are quoted relative to tetramethylsilane ($\delta = 0.00$) as internal standards. High-resolution atmospheric pressure chemical ionization time-of-flight (APCI-TOF) mass spectra were collected on a Bruker compact QTOF. UV-vis absorption spectra were recorded on a JASCO V-770 UV-vis spectrometer, whereas the fluorescence spectra and the photoluminescent quantum yield (PLQY) were recorded on a JASCO FP-8500 luminescence spectrophotometer. UV-vis and PL spectra were measured in thin films coated onto glass substrates. DSC and TG-DTA measurements were performed on a Hitachi High-Tech EXSTAR6000 DSA6220 and Hitachi High-Tech EXSTAR6000 TG/DTA6200 at a scan rate of 10 °C min^{-1}. X-ray diffraction measurements were performed on a Rigaku SmartLab. A OLYMPUS BX53M optical and polarizing optical microscope equipped with a Mettler FP90/82HT hot stage was used for visual observations of the optical textures. All reagents, all naphthalene derivatives, and solvents were purchased from FUJIFILM Wako Pure Chemical Co., Tokyo Chemical Industry Co., Ltd., Kanto Chemical Co., Inc., or Sigma Aldrich, and were used as received. **L-Val-PMDI** was prepared according to previous reports.[1]

Synthesis of BR-L-Val-PMDI (1)
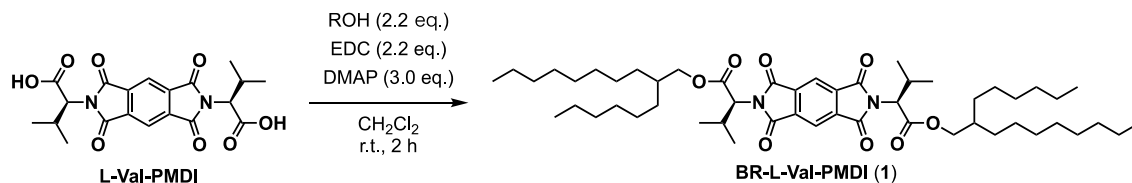
To a flask charged with **L-Val-PMDI** (1.04 g, 2.50 mmol) in CH_2Cl_2 (50 mL), 2-hexyl-1-decanol (1.33 g, 5.49 mmol), 1-ethyl-3-(3-dimethylaminopropyl)carbodiimide hydrochloride (EDC, 1.05 g, 5.48 mmol), and 4-dimethylaminopyridine (DMAP, 0.916 g, 7.50 mmol) were added at room temperature. The resulting mixture was stirred at room temperature for 2 h. After the addition of deionized water, the resulting mixture was extracted with $CHCl_3$ (3 times) and the combined organic layer was dried over Na_2SO_4, filtered, and evaporated. The residual oil was purified by column chromatography (silica gel) with $CHCl_3$/hexane (10:1) as the eluent to give **BR-L-Val-PMDI (1)** (1.12 g, 1.29 mmol, 52%) as a colorless oil (R_f = 0.80).

1: ^{1}H NMR (400 MHz, $CDCl_3$) δ 8.32 (s, 2H, Ha), 4.63 (d, J = 8 Hz, 2H, Hb), 4.05 (d, J = 6 Hz, 4H, Hc), 2.80 (dh, J = 14, 7 Hz, 2H, Hd), 1.61–1.52 (m, 2H, He), 1.32–1.14 (m, 54H, Hf and Hg or Hi), 0.92 (d, J = 7 Hz, 6H, Hg or Hi), 0.88 (t, J = 7 Hz, 6H, Hj or Hk), 0.86 (t, J = 7 Hz, 6H, Hj or Hk); ^{13}C{^{1}H} NMR (101 MHz, $CDCl_3$) δ 168.3 (C), 165.6 (C), 137.0 (C), 118.8 (CH), 68.5 (O–CH_2), 58.6 (N–CH), 37.2 (O(CH_2)CH), 31.9 (CH_2), 31.7 (CH_2), 31.2 (CH_2), 29.9 (CH_2), 29.6 (CH_2), 29.5 (CH_2), 29.3 (CH_2), 28.5 ($CH(CH_3)_2$), 26.6 (CH_2), 26.6 (CH_2), 26.5 (CH_2), 22.7 (CH_2), 22.6, (CH_2) 21.0 (CH_3), 19.6 (CH_3), 14.1 (CH_3), 14.1 (CH_3). HRMS (ESI), m/z: Found: 865.6284 ([M+H]$^+$), Calcd. for $C_{52}H_{85}N_2O_8$ ([M+H]$^+$): 865.6300.
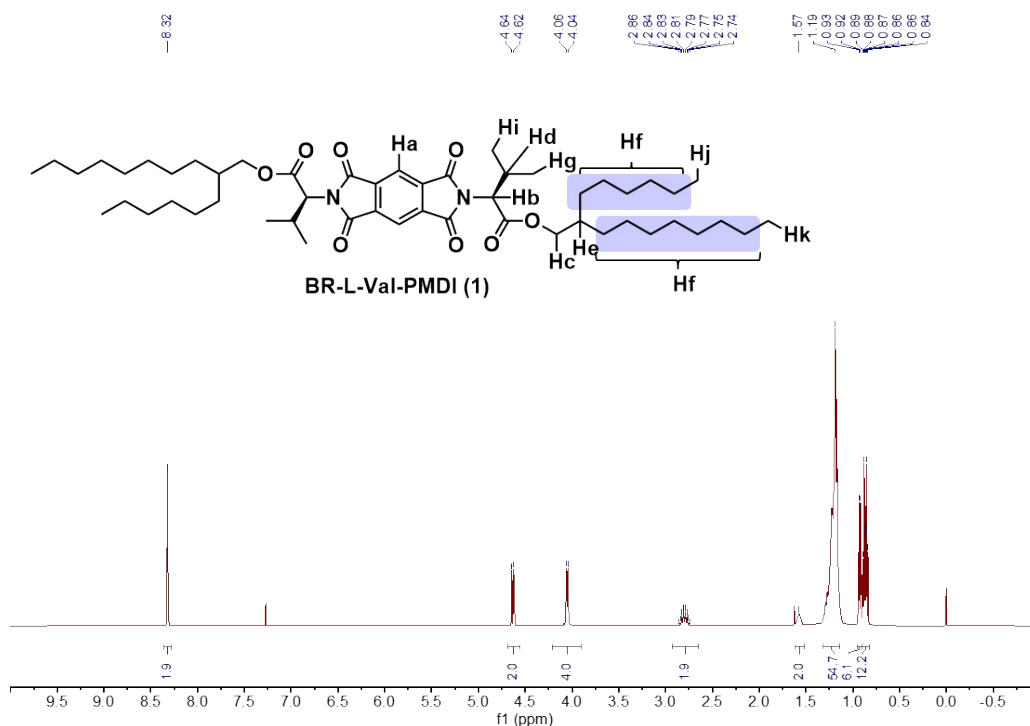
Figure S1-1. ^{1}H NMR spectrum of **BR-L-Val-PMDI (1)** in CDCl[3].
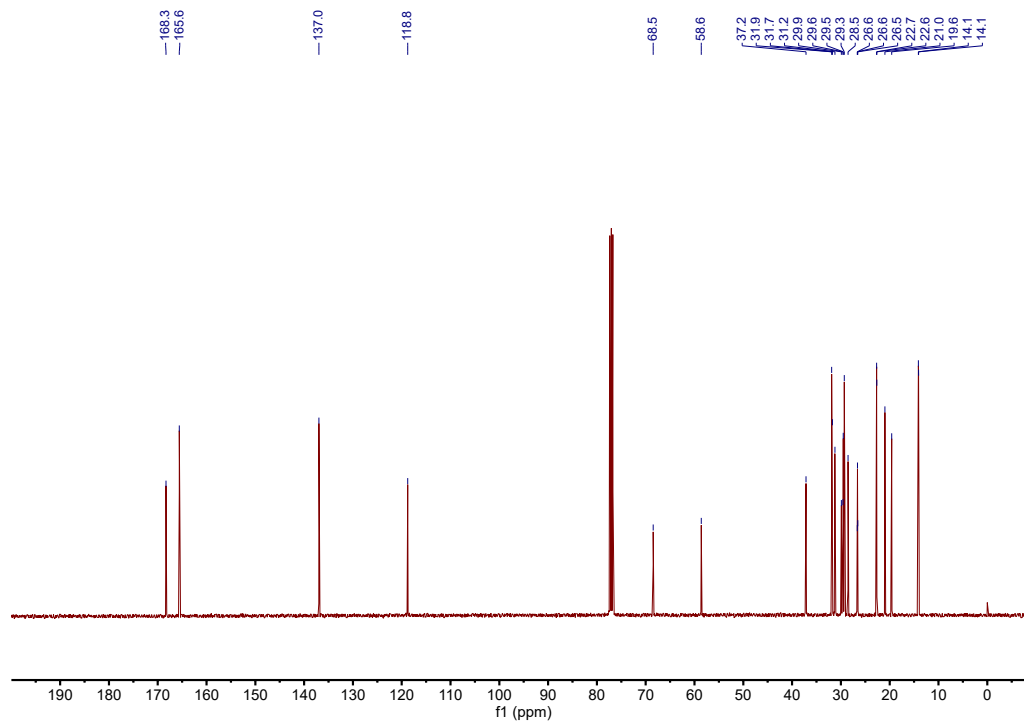
Figure S1-2. ^{13}C{^{1}H} NMR spectrum of **BR-L-Val-PMDI (1)** in CDCl[3].

S2. Crystal Structure Determination

Co-crystal was obtained by recrystallization of **L-Val-PMDI** and naphthalene (**NA-H**) from AcOEt. Crystallographic data for are summarized in Tables S1. Intensity data were collected on a Rigaku XtaLAB Synergy system using Cu-$K\alpha$ radiation (λ = 1.54184 Å). The structures were solved using the *SHELXT* program (*ver.* 2018/2)[2] and refined by a full-matrix least-squares method on F^2 for all reflections using the *SHELXL* program (*ver.* 2018/3 or 2019/3).[3] All non-hydrogen atoms were refined anisotropically, and the positions of all hydrogen atoms were calculated geometrically and refined as riding models. Supplementary crystallographic data were deposited at the Cambridge Crystallographic Data Centre (CCDC) under deposition numbers CCDC-2373409 (**L-Val-PMDI**) and CCDC-2353953 (**L-Val-PMDI·NA-H**) can be obtained free of charge via www.ccdc.cam.ac.uk/data_request.cif.

Table S2-1. Crystallographic data of **L-Val-PMDI** and its **NA-H** complex.

Compound	**L-Val-PMDI**	**L-Val-PMDI·NA-H**
Formula	$C_{20}H_{20}N_2O_8$	$C_{20}H_{20}N_2O_8(C_{10}H_8)$
Molecular Weight	416.38	544.54
Temperature / ºC	−173	−173
λ / Å	1.54184	1.54184
Crystal size / mm	$0.3 \times 0.2 \times 0.05$	$0.2 \times 0.15 \times 0.02$
Crystal system	Monoclinic	Monoclinic
Space group	$C2_1$ (#5)	$P2_1$ (#4)
a / Å	28.6709(4)	7.55420(10)
b / Å	5.29200(10)	7.02420(10)
c / Å	13.0480(2)	24.7028(3)
α / º	90	90
β / º	100.4960(10)	96.9480(10)
γ / º	90	90
V / Å^3	1946.60(5)	1301.16(3)
Z	4	2
μ / mm^{-1}	0.943	0.844
$D_{calcd.}$ / g·cm^{-3}	1.421	1.390
θ_{max} / º	72.620	72.906
Data/restr./param.	3749/1/277	5020/1/367
Completeness / %	100.0	100.0
GOF	1.058	1.033
R_1 (I>2σ(I))	0.0264	0.0257
wR_2 (I>2σ(I))	0.0705	0.0698
R_1 (all data)	0.0270	0.0259
wR_2 (all data)	0.0711	0.0701
Largest diff. peak and hole / e·Å^{-3}	0.280, 0.163	0.179, −0.201
CCDC number	2373409	2353953
Solv. for crystallization	Acetone, r.t.	AcOEt, r.t.

S3. Experimental data

S3-1. NA-H
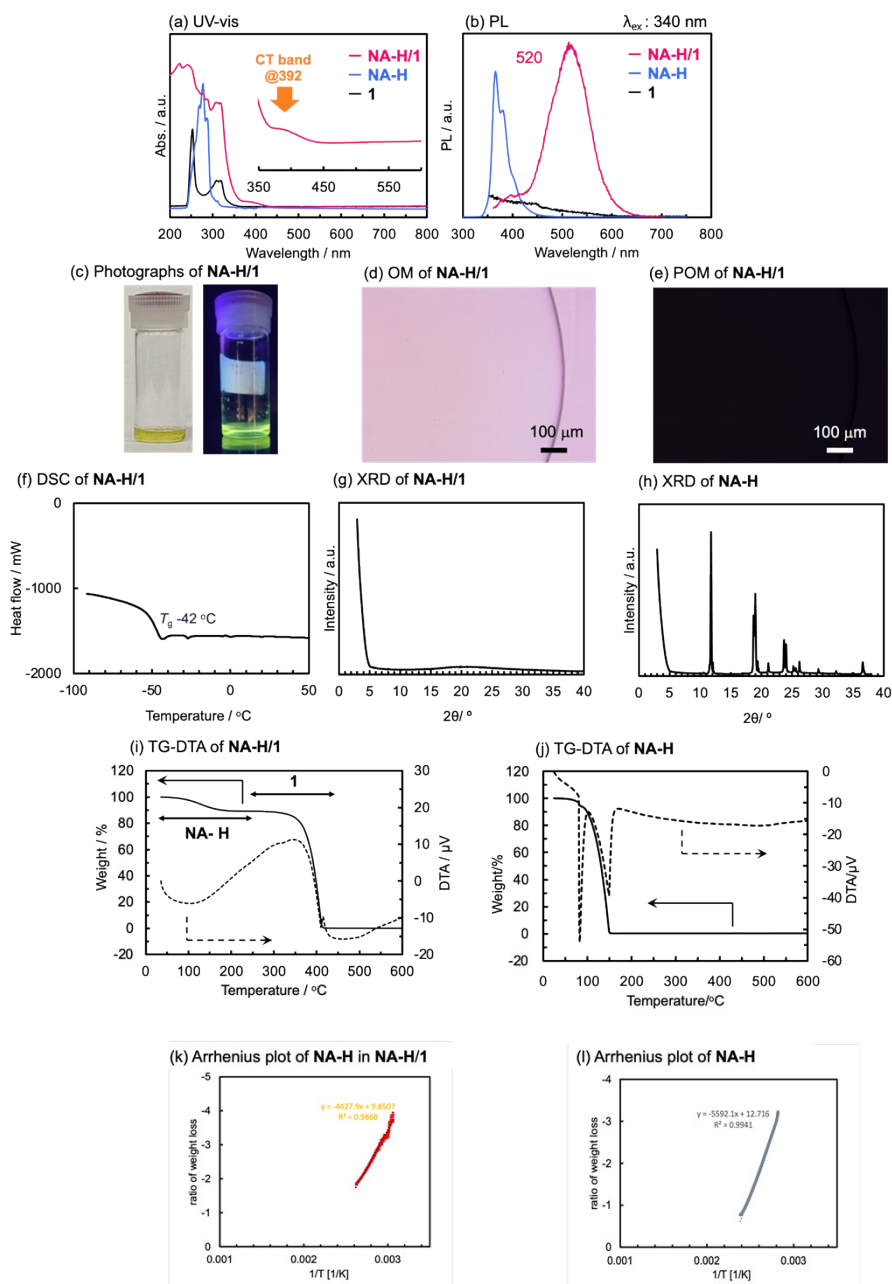
Figure S3-1. (a) UV-vis absorption and (b) PL spectra of **NA-H/1**, **NA-H**, and **1**. (c) Photographs of **NA-H/1** under room light (left) and black light (right) at r.t. (d and e) OM and POM observations of **NA-H/1** at r.t. (f) DSC traces of **NA-H/1** on 2nd heating at a scanning velocity of 10 $^{\circ}$C/min. (g and h) XRD patterns of **NA-H/1** and **NA-H** at r.t. (i and j) TG-DTA traces of **NA-H** and **NA-H/1** under N_2 atmosphere. (k and l) Temperature dependences for weight loss due to vaporization process of **NA-H** (InW vs T^{-1}) at 10 K/min heating rate under N_2 atmosphere. These plots correspond to the range of weight loss of **NA-H**. The values shown in the figure indicate activation energies of each condition.

S3-2. NA-N(CH₃)₂
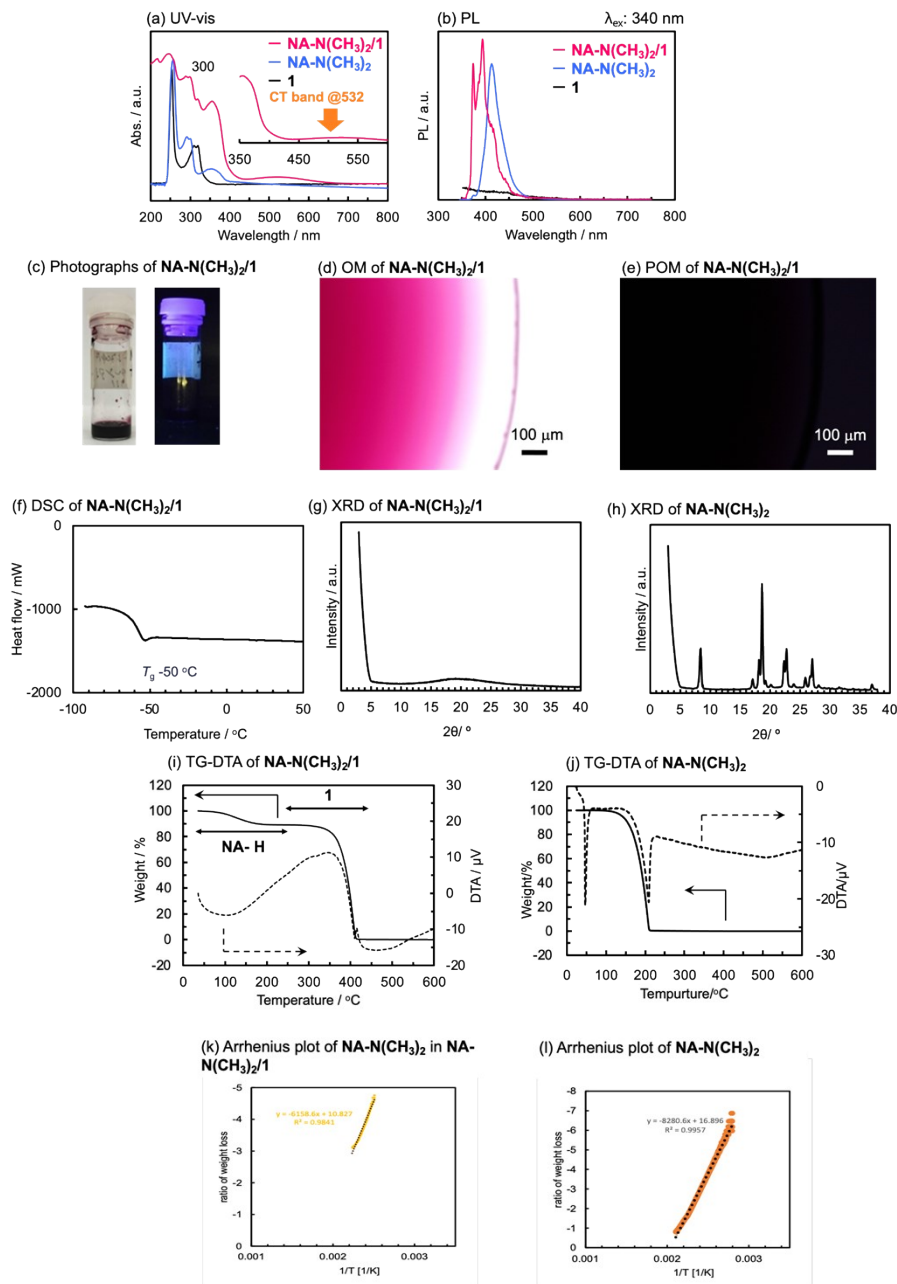
Figure S3-2. (a) UV-vis absorption and (b) PL spectra of **NA-N(CH₃)₂/1**, **NA-N(CH₃)₂**, and **1**. (c) Photographs of **NA-N(CH₃)₂/1** under room light (left) and black light (right) at r.t. (d and e) OM and POM observations of **NA-N(CH₃)₂** at r.t. (f) DSC traces of **NA-N(CH₃)₂/1** on 2nd heating at a scanning velocity of 10 °C/min. (g and h) XRD patterns of **NA-N(CH₃)₂/1** and **NA-N(CH₃)₂** at r.t. (i and j) TG-DTA traces of **NA-N(CH₃)₂** and **NA-N(CH₃)₂/1** under N₂ atmosphere. (k and l) Temperature dependences for weight loss due to vaporization process of **NA-N(CH₃)₂** (InW vs T^{-1}) at 10 K/min heating rate under N₂ atmosphere. These plots correspond to the range of weight loss of **NA-N(CH₃)₂**. The values shown in the figure indicate activation energies of each condition.

S3-3. NA-OCH₃
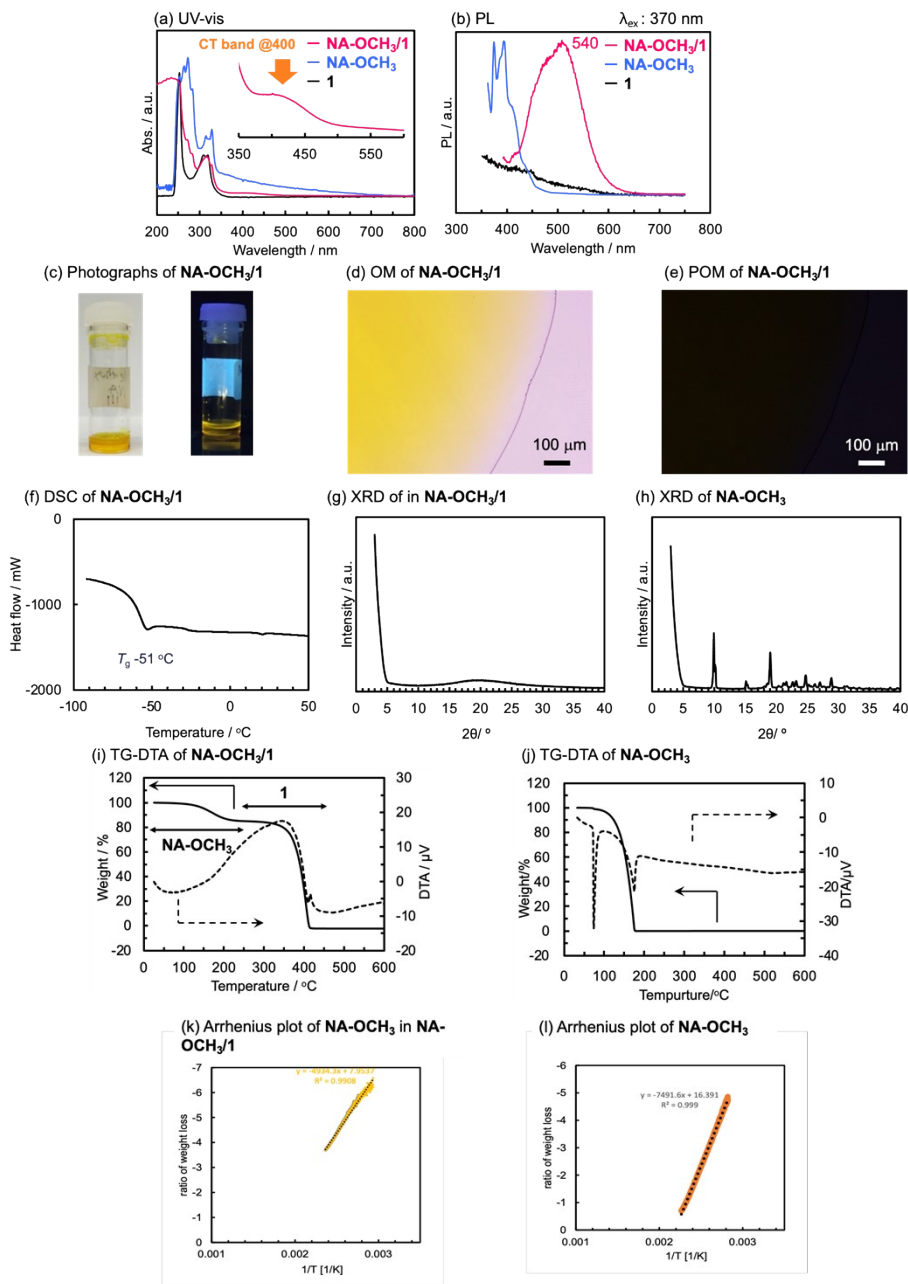
Figure S3-3. (a) UV-vis absorption and (b) PL spectra of **NA-OCH₃/1**, **NA-OCH₃**, and **1**. (c) Photographs of **NA-OCH₃/1** under room light (left) and black light (right) at r.t. (d and e) OM and POM observations of **NA-OCH₃** at r.t. (f) DSC traces of **NA-OCH₃/1** on 2nd heating at a scanning velocity of 10 °C/min. (g and h) XRD patterns of **NA-OCH₃/1** and **NA-OCH₃** at r.t. (i and j) TG-DTA traces of **NA-OCH₃** and **NA-OCH₃/1** under N_2 atmosphere. (k and l) Temperature dependences for weight loss due to vaporization process of **NA-OCH₃** ($\ln W$ vs T^{-1}) at 10 K/min heating rate under N_2 atmosphere. These plots correspond to the range of weight loss of **NA-OCH₃**. The values shown in the figure indicate activation energies of each condition.

S3-4. NA-CH₃
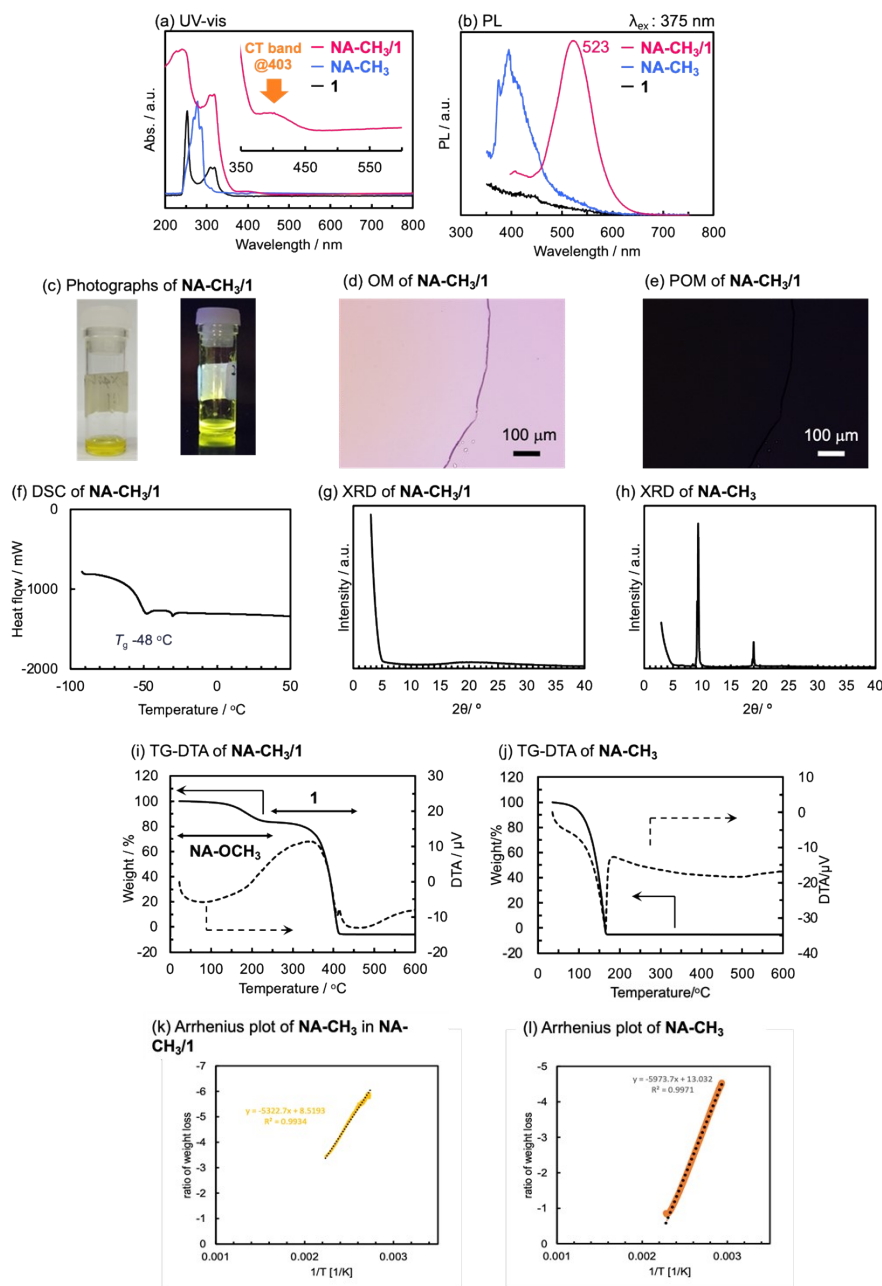
Figure S3-4. (a) UV-vis absorption and (b) PL spectra of **NA-CH₃/1**, **NA-CH₃**, and **1**. (c) Photographs of **NA-CH₃/1** under room light (left) and black light (right) at r.t. (d and e) OM and POM observations of **NA-CH₃** at r.t. (f) DSC traces of **NA-CH₃/1** on 2nd heating at a scanning velocity of 10 °C/min. (g and h) XRD patterns of **NA-CH₃/1** and **NA-CH₃** at r.t. (i and j) TG-DTA traces of **NA-CH₃** and **NA-CH₃/1** under N₂ atmosphere. (k and l) Temperature dependences for weight loss due to vaporization process of **NA-CH₃** (ln$W$ vs T^{-1}) at 10 K/min heating rate under N₂ atmosphere. These plots correspond to the range of weight loss of **NA-CH₃**. The values shown in the figure indicate activation energies of each condition.

S3-5. NA-Cl
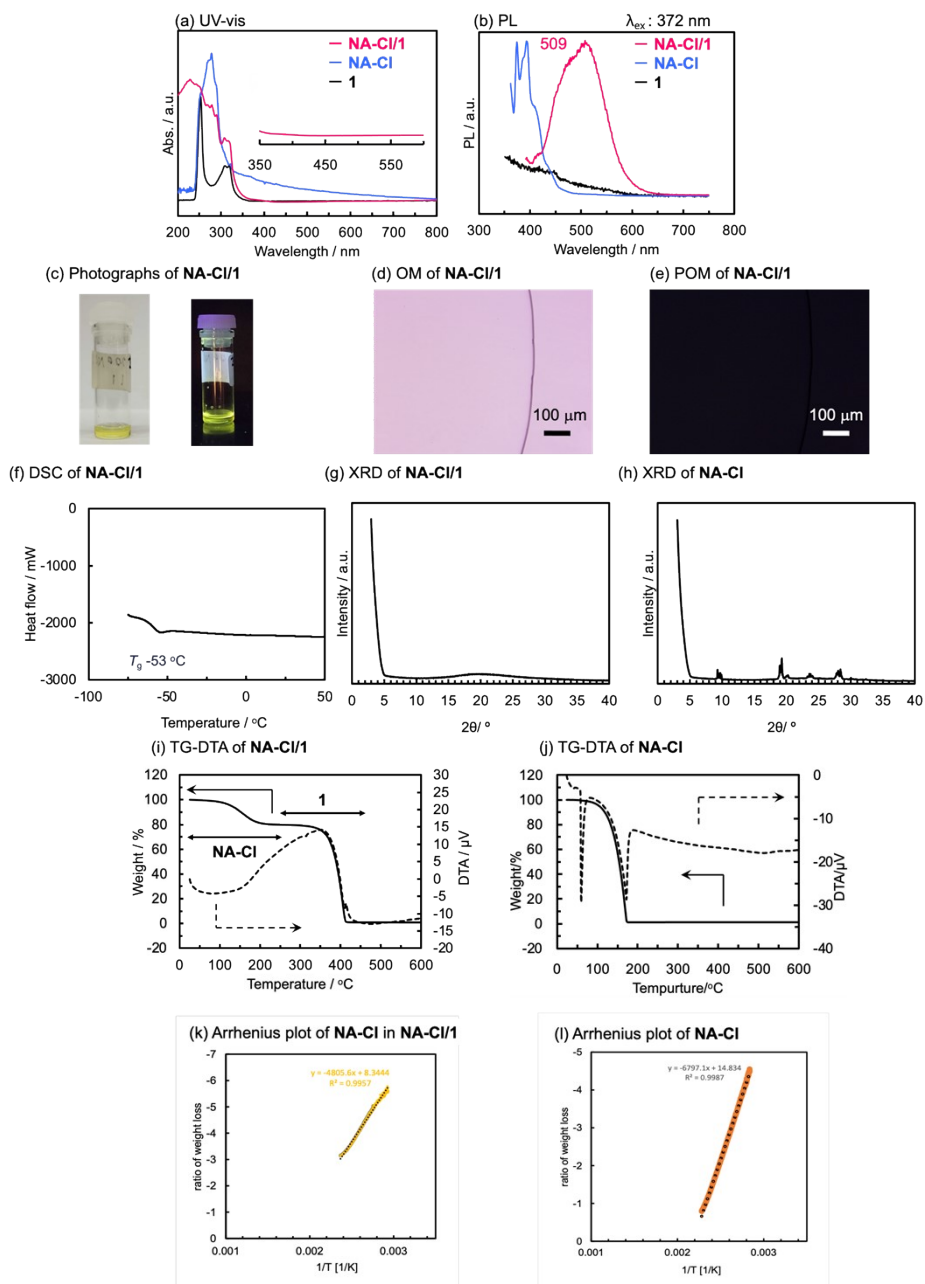
Figure S3-5. (a) UV-vis absorption and (b) PL spectra of **NA-Cl/1**, **NA-Cl**, and **1**. (c) Photographs of **NA-Cl/1** under room light (left) and black light (right) at r.t. (d and e) OM and POM observations of **NA-Cl** at r.t. (f) DSC traces of **NA-Cl/1** on 2nd heating at a scanning velocity of 10 °C/min. (g and h) XRD patterns of **NA-Cl/1** and **NA-Cl** at r.t. (i and j) TG-DTA traces of **NA-Cl** and **NA-Cl/1** under N_2 atmosphere. (k and l) Temperature dependences for weight loss due to vaporization process of **NA-Cl** ($\ln W$ vs T^{-1}) at 10 K/min heating rate under N_2 atmosphere. These plots correspond to the range of weight loss of **NA-Cl**. The values shown in the figure indicate activation energies of each condition.

S3-6. NA-COCH₃
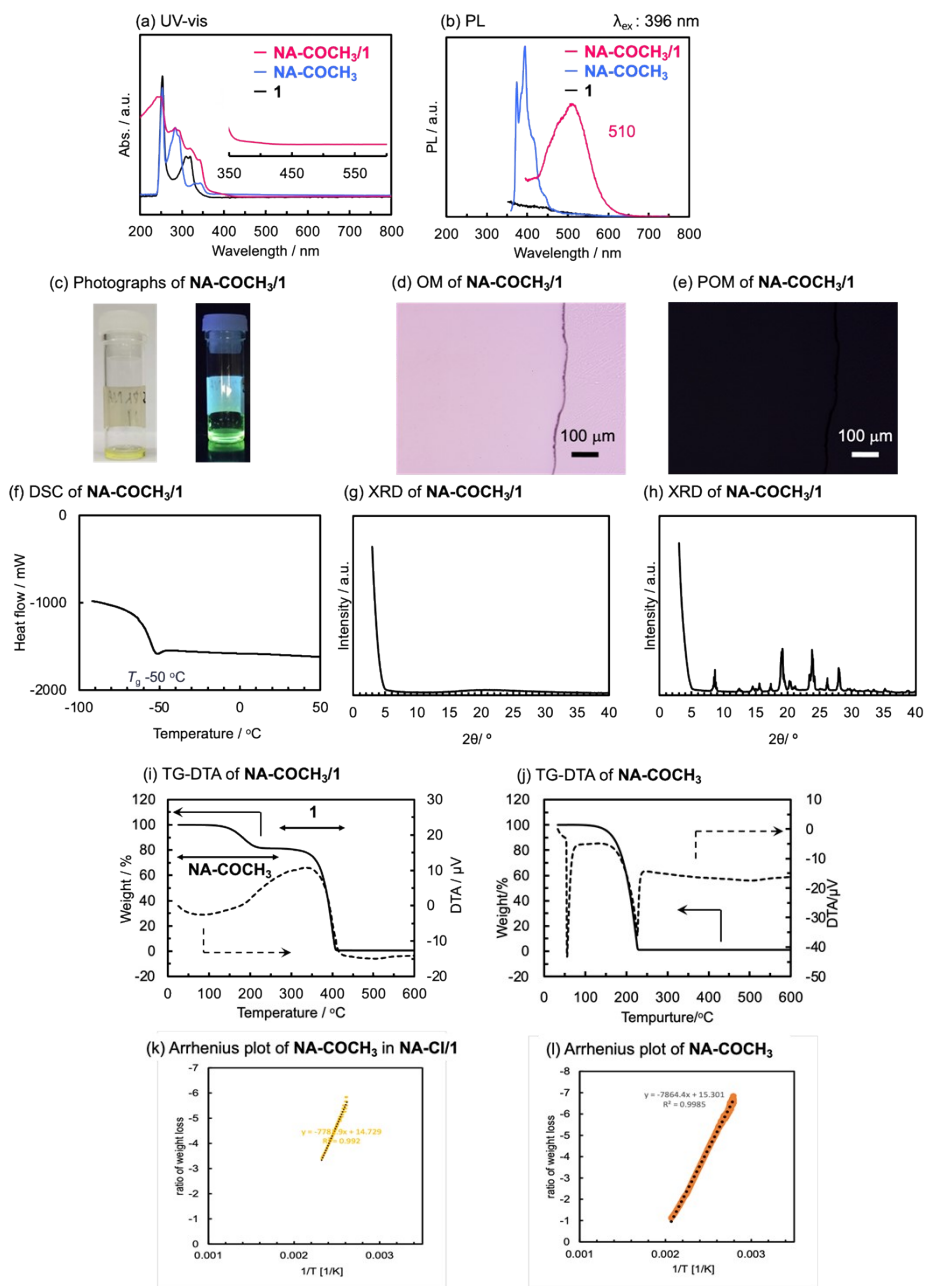
Figure S3-6. (a) UV-vis absorption and (b) PL spectra of **NA-COCH₃/1**, **NA-COCH₃**, and **1**. (c) Photographs of **NA-COCH₃/1** under room light (left) and black light (right) at r.t. (d and e) OM and POM observations of **NA-COCH₃** at r.t. (f) DSC traces of **NA-COCH₃/1** on 2nd heating at a scanning velocity of 10 °C/min. (g and h) XRD patterns of **NA-COCH₃/1** and **NA-COCH₃** at r.t. (i and j) TG-DTA traces of **NA-COCH₃** and **NA-COCH₃/1** under N_2 atmosphere. (k and l) Temperature dependences for weight loss due to vaporization process of **NA-COCH₃** ($\ln W$ vs T^{-1}) at 10 K/min heating rate under N_2 atmosphere. These plots correspond to the range of weight loss of **NA-COCH₃**. The values shown in the figure indicate activation energies of each condition.

S3-7. NA-COOCH₃
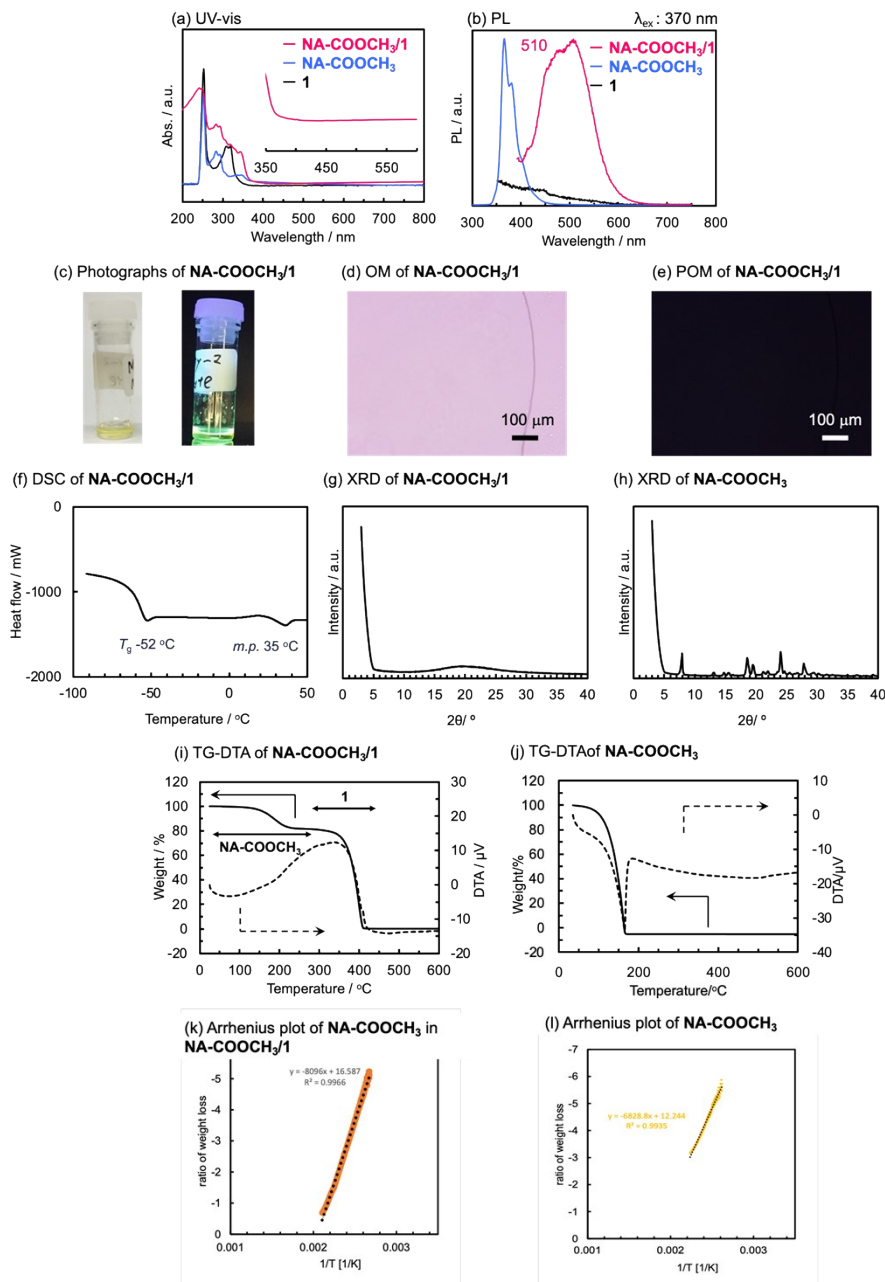
Figure S3-7. (a) UV-vis absorption and (b) PL spectra of **NA-COOCH₃/1**, **NA-COOCH₃**, and **1**. (c) Photographs of **NA-COOCH₃/1** under room light (left) and black light (right) at r.t. (d and e) OM and POM observations of **NA-COOCH₃** at r.t. (f) DSC traces of **NA-COOCH₃/1** on 2nd heating at a scanning velocity of 10 °C/min. (g and h) XRD patterns of **NA-COOCH₃/1** and **NA-COOCH₃** at r.t. (i and j) TG-DTA traces of **NA-COOCH₃** and **NA-COOCH₃/1** under N_2 atmosphere. (k and l) Temperature dependences for weight loss due to vaporization process of **NA-COOCH₃** ($\ln W$ vs T^{-1}) at 10 K/min heating rate under N_2 atmosphere. These plots correspond to the range of weight loss of **NA-COOCH₃**. The values shown in the figure indicate activation energies of each condition.

S3-8. NA-COH
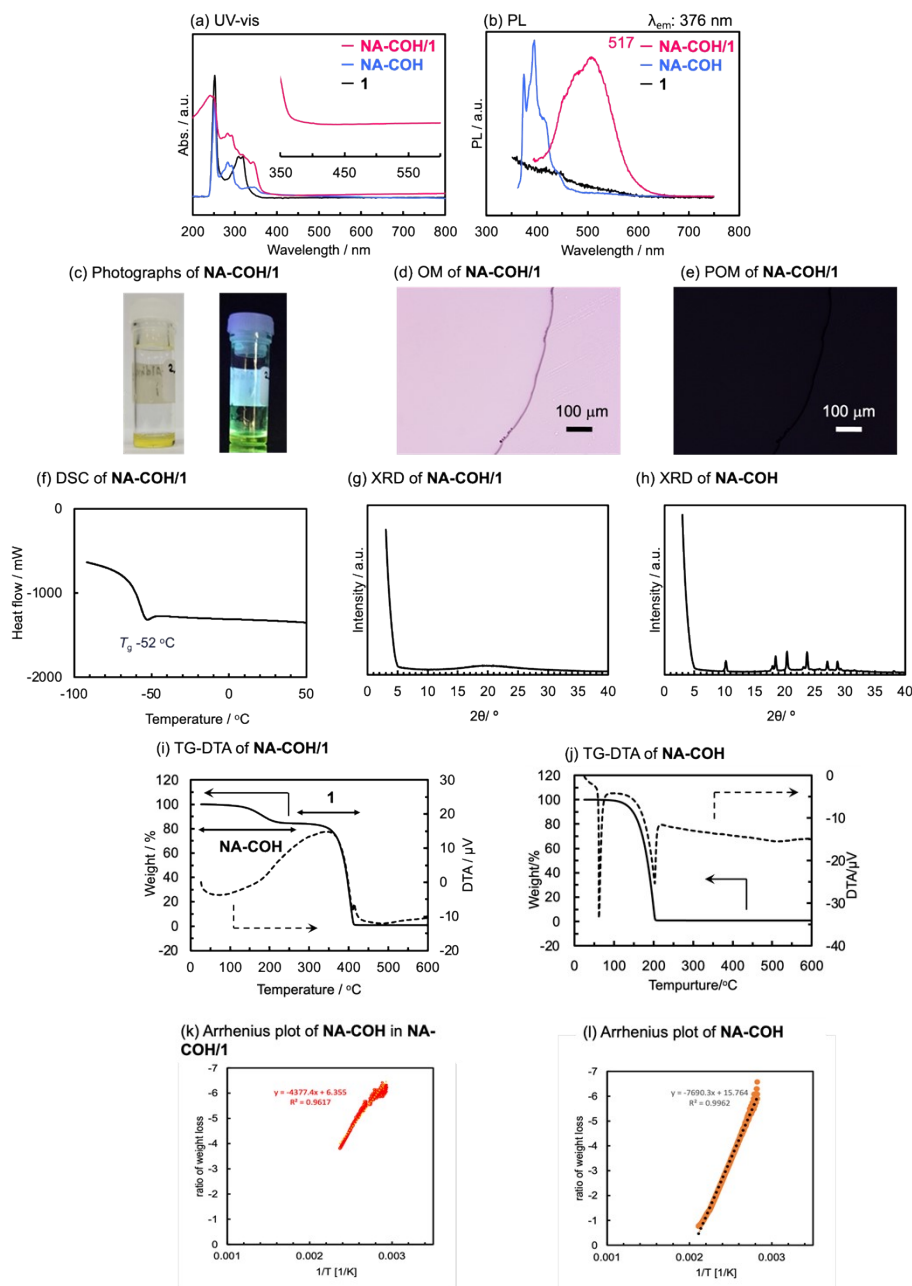
Figure S3-8. (a) UV-vis absorption and (b) PL spectra of **NA-COH/1**, **NA-COH**, and **1**. (c) Photographs of **NA-COH/1** under room light (left) and black light (right) at r.t. (d and e) OM and POM observations of **NA-COH** at r.t. (f) DSC traces of **NA-COH/1** on 2nd heating at a scanning velocity of 10 °C/min. (g and h) XRD patterns of **NA-COH/1** and **NA-COH** at r.t. (i and j) TG-DTA traces of **NA-COH** and **NA-COH/1** under N_2 atmosphere. (k and l) Temperature dependences for weight loss due to vaporization process of **NA-COH** (ln$W$ vs T^{-1}) at 10 K/min heating rate under N_2 atmosphere. These plots correspond to the range of weight loss of **NA-COH**. The values shown in the figure indicate activation energies of each condition.

S3-9. NA-CN
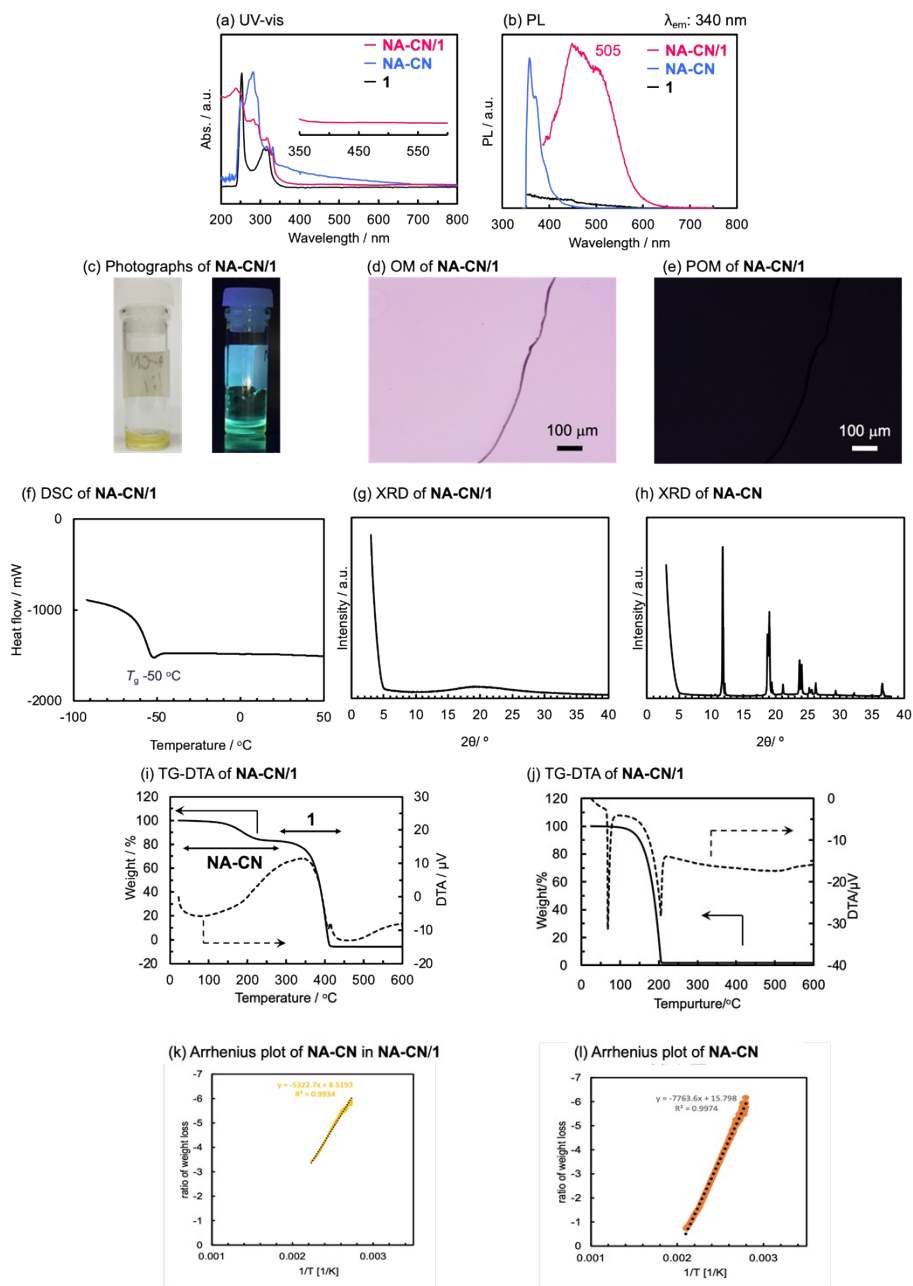
Figure S3-9. (a) UV-vis absorption and (b) PL spectra of **NA-CN/1**, **NA-CN**, and **1**. (c) Photographs of **NA-CN/1** under room light (left) and black light (right) at r.t. (d and e) OM and POM observations of **NA-CN** at r.t. (f) DSC traces of **NA-CN/1** on 2nd heating at a scanning velocity of 10 °C/min. (g and h) XRD patterns of **NA-CN/1** and **NA-CN** at r.t. (i and j) TG-DTA traces of **NA-CN** and **NA-CN/1** under N_2 atmosphere. (k and l) Temperature dependences for weight loss due to vaporization process of **NA-CN** (ln$W$ vs T^{-1}) at 10 K/min heating rate under N_2 atmosphere. These plots correspond to the range of weight loss of **NA-CN**. The values shown in the figure indicate activation energies of each condition.
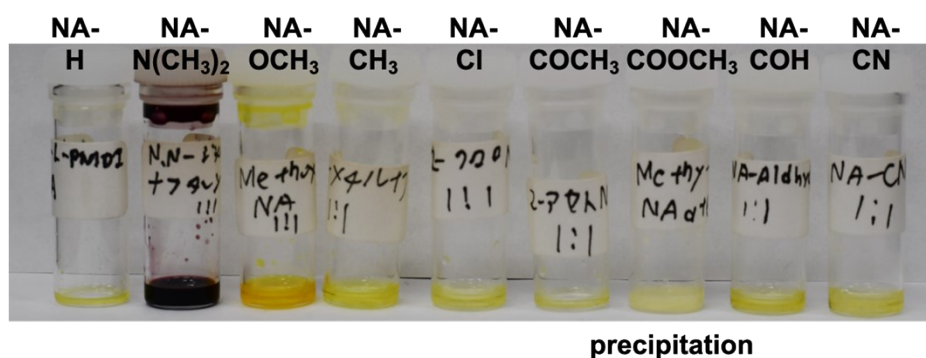
precipitation

Figure S3-10. Photographs of **NA-#/1** cooled after 2h. All **NA-#/1** adapt solution states cooled after 2h except with **NA-COOCH₃/1** in this experimental conditions. For **NA-COOCH₃/1**, the precipitation was observed, however, heating process can recover into solution state, immediately.

S3-11. BR-L-Val-PMDI (1)
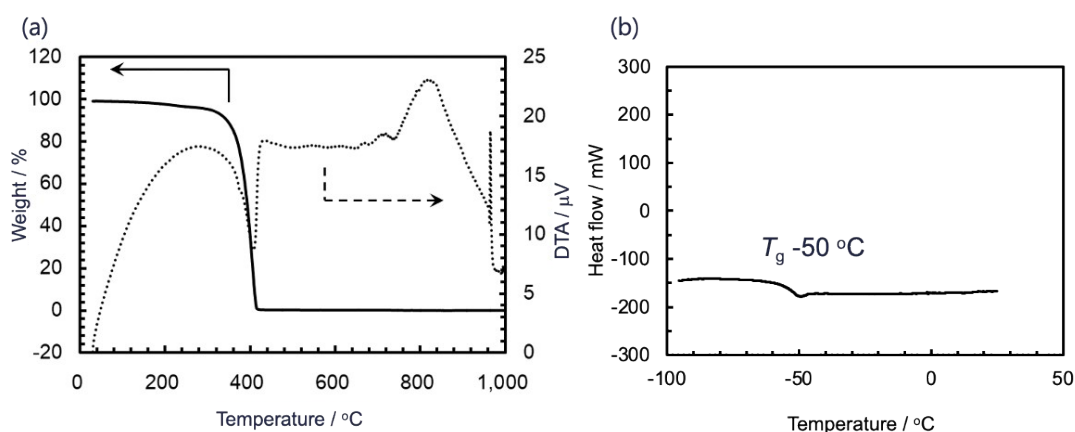
Figure S3-11. (a) TG-DTA trace of **1** under N_2 atmosphere. (b) DSC traces of **1** on 2nd heating at a scanning velocity of 1 °C/min.

S3-12. Summary

Table S3-1. Summary of photophysical and electronic properties and ΔE of **NA-#s** and **NA-#s/1**.

NA-#s	UV-vis / nm	PL / nm	CT / nm	Ex. / nm	HOMO / eV ^{a}	LUMO / eV ^{a}	$\Delta E_{\text{NA-#s}}$ / kJ/mol ^{b}	$\Delta E_{\text{NA-#s/1}}$ / kJ/mol ^{c}	PLQY / %
NA-N(CH$_3$)$_2$	300,530	390	532	340	-4.91	-0.65	68.9	51.2	0.4
NA-CH$_3$	320	523	403	279,376	-5.70	-0.86	49.7	44.3	0.9
NA-OCH$_3$	320,420	540	400	370	-5.42	-0.90	62.3	41	2.8
NA-H	320	520	392	279	-5.79	-0.96	46.6	36.8	7.5
NA-Cl	278	509	-	372	-6.04	-1.27	56.5	40	1.8
NA-COCH$_3$	300	510	-	372	-6.12	-1.72	64.5	64.7	1.7
NA-CO$_2$CH$_3$	336	510	-	370	-6.72	-1.72	67.3	56.8	2.3
NA-COH	340	517	-	376	-6.25	-1.88	63.9	48	1.8
NA-CN	330	505	-	280,370	-6.39	-1.81	64.5	44.3	2.4
Me-L-Val-PMDI					-7.39	-3.01			

^{a} calculated with a B3LYP-D3(BJ) functional using 6-31G(d,p) basis sets.

^{b} calculated activation energy of **NA-#s** according to **S5**.

^{c} calculated activation energy of **NA-#s** in **NA-#s/1** according to **S5**.
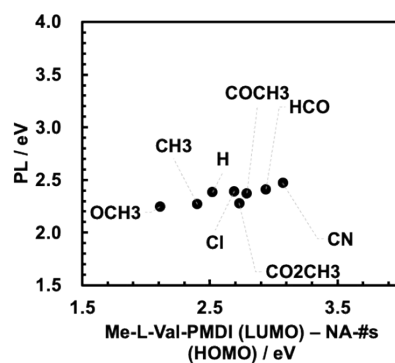
Figure S3-12. The relationship between peaks in PL spectra and HOMO-LUMO gap estimated by DFT calculations.

S4. Computational Details

BR-L-Val-PMDI (1)   **Me-L-Val-PMDI (2)**
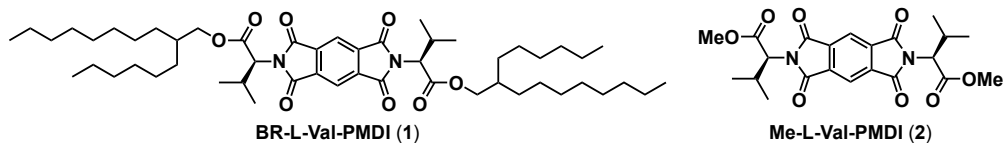
To obtain details of the electronic structure of **1·NA-H** complex, computational studies were carried out by using the model compound **Me-L-Val-PMDI (2)**. The molecular structure of **L-Val-PMDI·NA-H** complex obtained from a single-crystal X-ray diffraction analysis was used as an initial structure of the model compound **2·NA-H** complex in which CO_2H groups were replaced by CO_2Me. All calculations were performed in the gas phase using the *Gaussian 16* program package (Rev. C.01).[4] The ground-state geometry optimization of **2·NA-H** was carried out with a B3LYP-D3(BJ) functional[5] using 6-31G(d,p) basis sets. After each geometry optimization, a frequency calculation at the same level was performed to verify that all the stationary points had no imaginary frequency. Interaction energy in **2·NA-H** complex summarized in Table S4-1 was evaluated through single point calculation with counterpoise correction at the B3LYP-D3(BJ)/6-311+G(d,p) level of theory.[6] The time-dependent density functional theory (TD-DFT)[7] calculation was performed with a CAM-B3LYP-D3(BJ) functional[8] using 6-31+G(d,p) basis sets. The result for TD-DFT calculation is summarized in Table S4-2 and Figure S4-1.

Table S4-1. Interaction energy in **2·NA-H** (kcal/mol).

	raw	corrected	BSSE
2·NA-H	−17.55	−15.20	2.35

Table S4-2. Calculated wavelengths for the absorption spectrum of **2·NA-H** complex, its oscillator strengths, and the associated transitions with |CI coefficient| > 0.2.

Wavelength (nm)	Oscillator strength	MO contribution			CI coefficient
376	0.0263	HOMO	→	LUMO	0.7046
		HOMO–5	→	LUMO	0.31684
		HOMO–4	→	LUMO	0.46265
		HOMO–3	→	LUMO	−0.21898
		HOMO–2	→	LUMO+1	0.22735
278	0.0289	HOMO	→	LUMO+1	0.68086
271	0.025	HOMO–1	→	LUMO+2	0.23191
		HOMO–1	→	LUMO+3	0.25429
		HOMO	→	LUMO+2	0.41143
		HOMO	→	LUMO+4	−0.33204

(a) HOMO–5

(b) HOMO–4

(c) HOMO–3

(d) HOMO–2

(e) HOMO–1

(f) HOMO

(g) LUMO

(h) LUMO+1

(i) LUMO+2

(j) LUMO+3

(k) LUMO+4
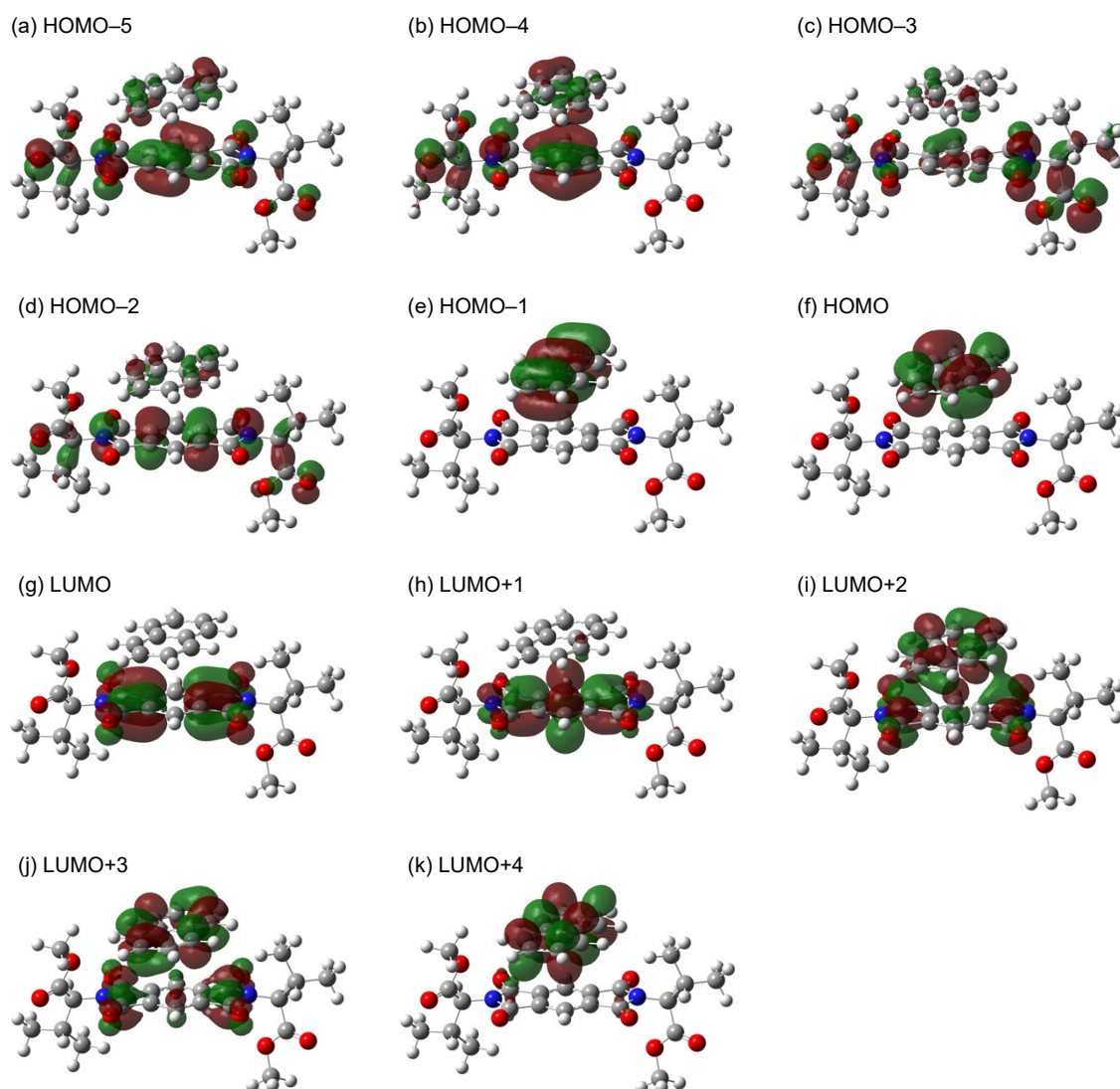
Figure S4-1. Selected molecular orbitals of **2·NA-H** complex at the CAM-B3LYP-D3(BJ)/6-31+G(d,p) level of theory. The molecular orbitals are drawn with a contour value of 0.03 atomic unit.

S5. Arrhenius plot

TG diagrams obtained using the heating method can be analyzed by reaction kinetics theory.[9] The sublimation rate v follows an Arrhenius trend as

$$\frac{dm}{dt} = v = A\exp\left(-\frac{\Delta E}{RT}\right)f(m) \qquad (1)$$

where m, A, ΔE, R, and T are mass loss rate, a pre-exponential factor, the activation energy, the universal real gas constant, and absolute temperature, respectively. $f(m)$ denotes $(1-m)^n$, and the parameter n is 1.0 when the sample is powder solids. Eq.(1) can be rewritten as

$$\ln v - n\ln(1-m) = -\left(\frac{\Delta E}{R}\right)\frac{1}{T} + \ln A \qquad (2)$$

The ΔE can be calculated from the slope of plots of $\ln v$–$n\ln(1-m)$ and $1/T$. Arrhenius plots of TG diagrams in Figure S3-1(g) to 9(g) were illustrated in Figure S3-1(h and i) to 9(h and i) by using the temperature range of vaporization for **NA-#s**, where the values of ΔE were determined in Table , respectively.

S6. Thermal-responsive behavior
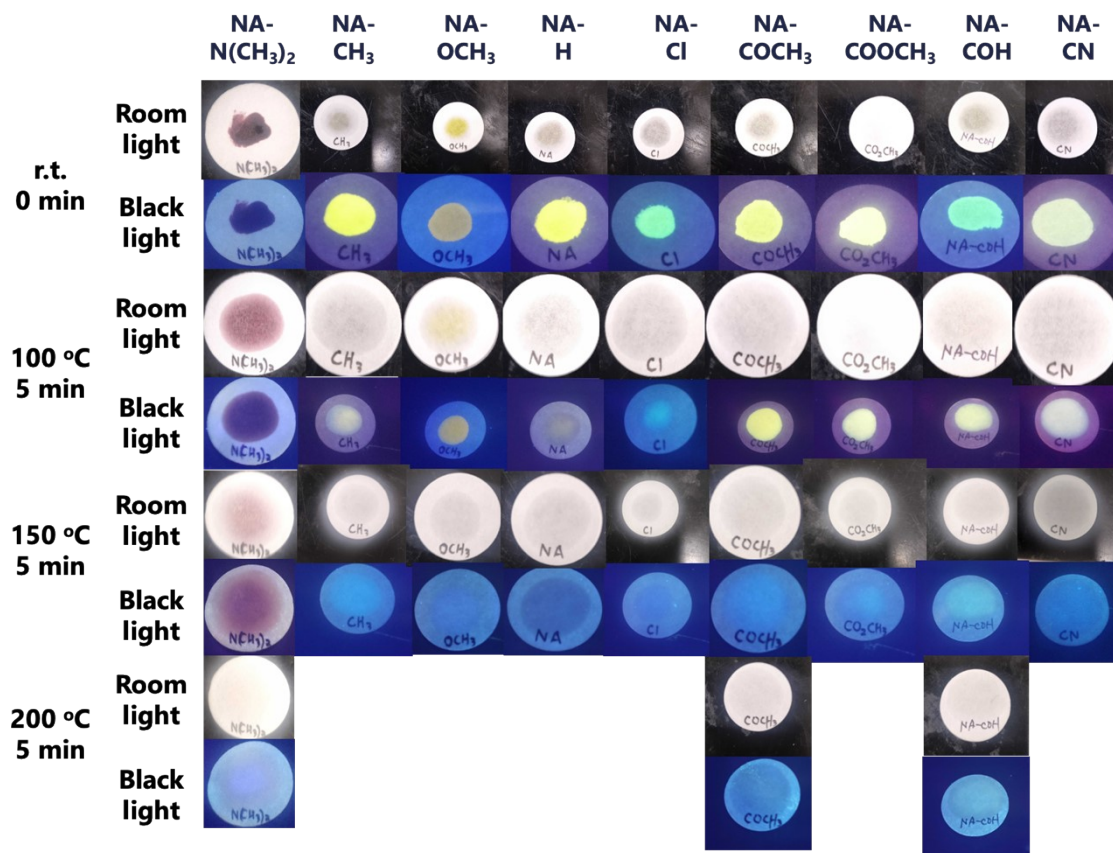
Figure S6-1. Thermal-responsive behaviors of **NA-#s/1** in response to heating at 100, 150, and 200 °C.

NA-#s/1 printed onto filter papers were heated on the hot plate at 100, 150, and 200 °C for 5 min.

For **NA-N(CH₃)₂/1**, **N(CH₃)₂** retained on the filter paper upon heating at 100 and 150 °C for 5 min, whereas

N(CH₃)₂ was vaporized at 200 °C for 5 min. Another **NA-#s/1** were similar behavior to **NA-N(CH₃)₂/1**.

References

1. K. Faghihi, M. Hajibeygi, M. Shabanian, *J. Macromol. Sci. Part A* **2010**, *47*, 144–153.

2. G. M. Sheldrick, *Acta Cryst.* **2015**, *A71*, 3–8.

3. G. M. Sheldrick, *Acta Cryst.* **2015**, *C71*, 3–8.

4. *Gaussian 16, Revision C.01*, M. J. Frisch, G. W. Trucks, H. B. Schlegel, G. E. Scuseria, M. A. Robb, J. R. Cheeseman, G. Scalmani, V. Barone, G. A. Petersson, H. Nakatsuji, X. Li, M. Caricato, A. V. Marenich, J. Bloino, B. G. Janesko, R. Gomperts, B. Mennucci, H. P. Hratchian, J. V. Ortiz, A. F. Izmaylov, J. L. Sonnenberg, D. Williams-Young, F. Ding, F. Lipparini, F. Egidi, J. Goings, B. Peng, A. Petrone, T. Henderson, D. Ranasinghe, V. G. Zakrzewski, J. Gao, N. Rega, G. Zheng, W. Liang, M. Hada, M. Ehara, K. Toyota, R. Fukuda, J. Hasegawa, M. Ishida, T. Nakajima, Y. Honda, O. Kitao, H. Nakai, T. Vreven, K. Throssell, J. A. Montgomery, Jr., J. E. Peralta, F. Ogliaro, M. J. Bearpark, J. J. Heyd, E. N. Brothers, K. N. Kudin, V. N. Staroverov, T. A. Keith, R. Kobayashi, J. Normand, K. Raghavachari, A. P. Rendell, J. C. Burant, S. S. Iyengar, J. Tomasi, M. Cossi, J. M. Millam, M. Klene, C. Adamo, R. Cammi, J. W. Ochterski, R. L. Martin, K. Morokuma, O. Farkas, J. B. Foresman, and D. J. Fox, Gaussian, Inc., Wallingford CT, 2019.

5. (a) A. D. Becke, *Phys. Rev. A: Gen. Phys.* **1988**, *38*, 3098–3100.
   (b) C. Lee, W. Yang, R. G. Parr, *Phys. Rev. B: Condens. Matter* **1988**, *37*, 785–789.
   (c) A. D. Becke, *J. Chem. Phys.* **1993**, *98*, 1372–1377.
   (d) A. D. Becke, *J. Chem. Phys.* **1993**, *98*, 5648–5652.

6. S. Grimme, S. Ehrlich, L. Goerigk, *J. Comp. Chem.* **2011**, *32*, 1456–1465.

7. (a) R. Bauernschmitt, R. Ahlrichs, *Chem. Phys. Lett.* **1996**, *256*, 454–464.
   (b) M. E. Casida, C. Jamorski, K. C. Casida, D. R. Salahub, *J. Chem. Phys.* **1998**, *108*, 4439–4449.

8. T. Yanai, D. Tew, N. Handy, *Chem. Phys. Lett.* **2004**, *393*, 51–57.

9. R. D. Chirico, S. E. Knipmeyer, A. Nguyen and W. V. Steele, *J. Chem. Thermodyn.* **1993**, *25*, 1461–1494.